OPTICA

Snapshot parallel refractive index tomography

Qianyi Wu,[1] Jie Hu,[1] Hongki Lee,[1] Junxiang Zhao,[1] Ming Lei,[1] and Zhaowei Liu[1,2,*]

[1]Department of Electrical and Computer Engineering, University of California, San Diego, 9500 Gilman Drive, La Jolla, California 92093, USA
[2]Materials Science and Engineering Program, University of California, San Diego, 9500 Gilman Drive, La Jolla, California 92093, USA
*zhaowei@ucsd.edu

Received 2 September 2025; revised 9 February 2026; accepted 11 February 2026; published 27 February 2026

Phase Imaging enables label-free visualization of transparent biological samples, offering critical insight into cellular structure and transient dynamics with minimal phototoxicity. However, existing three-dimensional (3D) phase imaging techniques typically require sequential scanning or interferometric setups, limiting temporal resolution and increasing system complexity. To overcome these challenges, we propose snapshot parallel refractive index tomography (SPRIT), a snapshot, 3D refractive index (RI) imaging technique. SPRIT employs a diffractive optical element to capture multifocal intensity images. The volumetric RI distribution is reconstructed by deconvolving the intensity measurement with the 3D transfer functions of the system. By incorporating partially coherent illumination, SPRIT achieves higher spatial resolution than coherent imaging systems, with the degree of enhancement governed by the illumination and detection numerical apertures. We demonstrate volumetric imaging of live *Chilomonas* at 50 Hz with SPRIT, showcasing its ability to resolve fine subcellular structures in real-time. With its snapshot, high-resolution capabilities, SPRIT offers a powerful tool for label-free 3D imaging in cellular biology and medical diagnostics. © 2026 Optica Publishing Group under the terms of the Optica Open Access Publishing Agreement

https://doi.org/10.1364/OPTICA.577676

1. INTRODUCTION

Imaging biological cells and tissues is crucial for advancing biological research and clinical diagnostics [1]. Many biological samples are weakly absorbing/scattering objects with a nonuniform spatial distribution of phase or refractive index (RI) [2,3]. Conventional phase microscopy [4,5] provides label-free contrast but offers only qualitative information. Over the past three decades, quantitative phase imaging (QPI) has emerged as a powerful tool for label-free imaging, offering precise measurement of optical phase with diverse implementations [6–8]. In addition to interferometric techniques [9–11], non-interferometric methods such as Fourier ptychography [12], transport of intensity equation (TIE) [13,14], and differential phase contrast (DPC) imaging [15] have gained attention, as they eliminate the need for complex interferometric setups and can recover phase information from intensity-only measurements. Furthermore, their compatibility with partially coherent illumination makes them attractive for cost-effective, robust imaging systems.

Recent advancements have extended non-interferometric techniques to volumetric RI imaging. Methods such as partially coherent intensity diffraction tomography (PC-IDT) [16–18] and 3D DPC [19] resolve 3D RI distributions from intensity data acquired through axial scanning. By exploiting the spatial frequency diversity introduced by the condenser aperture under partially coherent illumination [20,21], these methods enable 3D reconstruction via deconvolution, revealing internal structures that are inaccessible to conventional 2D QPI techniques. Compared with traditional coherent optical diffraction tomography (ODT) [22–24], these methods offer reduced speckle artifacts and avoid the need for complex angular scanning setups. However, they typically require the acquisition of hundreds of images, limiting their applicability in transient dynamic imaging scenarios.

Efforts have been made to accelerate quantitative phase imaging and reduce system complexity. Recent work has demonstrated snapshot 2D QPI methods based on modified Hartmann masks [25], metasurfaces [26–29], thin films [30], and diffractive surfaces [31]. To enable real-time 3D phase imaging, researchers have proposed single-shot tomographic techniques based on multiplexed off-axis holography [32,33] or light field imaging [34–36]. Multiplexed off-axis holography relies on the interference of multiple beams with different illumination angles to multiplex volumetric information in the frequency domain. However, it suffers from crosstalk among channels, speckle noise, and image quality degradation due to back-and-forth Fourier transform during reconstruction. Light field imaging employs the lenslet array, which divides the detection area into many sub-apertures, each producing an off-axis hologram corresponding to a unique illumination angle. The limited numerical aperture leads to degraded spatial resolution, both laterally and axially. Another important snapshot approach employs image-splitting prisms to generate multifocal images for 3D phase retrieval [37], though the 1D arrangement of a small number of planes may constrain axial sampling density and reconstruction quality.

In this work, we propose and experimentally demonstrate a snapshot 3D QPI method named snapshot parallel refractive index tomography (SPRIT). SPRIT parallelly captures a 2D grid of multifocal images generated by a diffractive optical element (DOE)

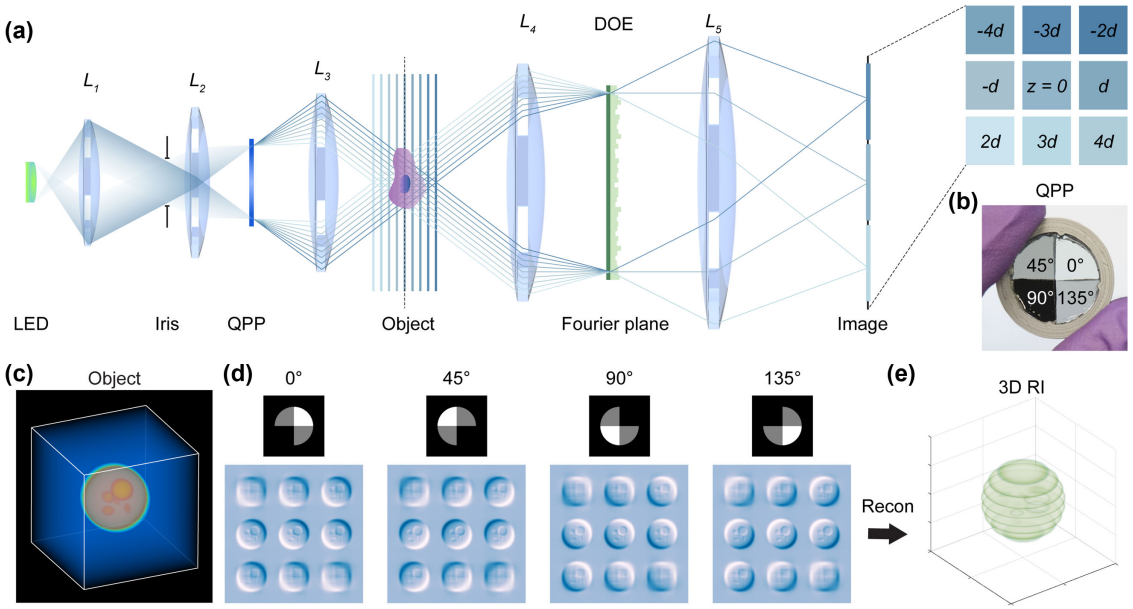

Fig. 1. Working principle of SPRIT. (a) Schematic of the SPRIT setup. L_1-L_5, lenses. A quadrant polarization plate (QPP) is placed at the front pupil plane of the condenser L_3 to generate polarization-dependent illumination with diverse spatial frequency components. The transmitted light is collected by the objective L_4. A diffractive optical element (DOE) positioned at the rear Fourier plane disperses and refocuses the sub-images at multiple axial depths. Marginal rays corresponding to each focal plane are shown. Inset, sub-images focused on nine planes (−4d to +4d) are formed simultaneously using a schematic 3 × 3 DOE. (b) A photograph of the custom QPP composed of four quadrantal polarized films with linear polarization orientations of 0°, 45°, 90°, and 135°. The QPP is placed in front of a liquid crystal display emitting light polarized at 0°. (c) A 3D phantom used for simulation. (d) Simulated raw measurements captured by the polarization camera, corresponding to four distinct illumination patterns. (e) Reconstructed refractive index slices using the 3D deconvolution.

placed at the Fourier plane of the imaging system. Meanwhile, the partially coherent illumination source of the system is polarization-multiplexed with a customized quadrant polarization plate (QPP). The multifocal images recorded by a polarization camera are rearranged to form four 3D image stacks, each corresponding to a unique transfer function. A 3D deconvolution algorithm utilizing either Tikhonov or total variation (TV) regularization prior is applied to retrieve the 3D RI distributions. We validate SPRIT with *Spirogyra* and live *Chilomonas* cells. SPRIT enables prolonged 3D imaging with both high temporal and spatial resolution, providing a powerful tool for observing ultrafast dynamics in complex biological systems and offering transformative potential for biomedical research.

2. METHODS

SPRIT captures four-channel image stacks containing spatially separated multifocal images, all within a single camera frame. The schematic of the SPRIT setup is illustrated in Fig. 1(a). A partially coherent LED source is utilized. To enable simultaneous acquisition of images illuminated by various source patterns, partial coherence multiplexing strategies based on color or polarization multiplexing have been previously demonstrated [38–40]. Here, we implement polarization multiplexing with a custom QPP [Fig. 1(b)] placed at the front Fourier plane of the imaging system. The four quadrants of the QPP are polarized with linear transmission orientations of 0°, 45°, 90°, and 135°. A polarization-insensitive DOE is positioned at the rear Fourier plane of the imaging system to create multifocal images. The DOE performs two key functions: first, it uniformly splits the transmitted light from the sample into distinct diffraction orders, generating an array of N × N images on the detector; second, it applies a defocus phase to each order, effectively refocusing the images to different axial depths, separated by a constant step size d. For instance, a schematic 3 × 3 DOE creates nine focal planes ranging from $-4d$ to $4d$, as shown in the inset of Fig. 1(a). Finally, a polarization camera, which contains interspersed polarized pixels with 0°, 45°, 90°, and 135° polarization orientations, enables simultaneous acquisition of image arrays under four distinct illumination conditions. The resulting raw image contains $4N^2$ sub-images, which can be segmented and rearranged to construct four 3D intensity stacks for RI reconstruction.

The forward model for image formation is derived under the first Born approximation [41] (see Section S1 of Supplement 1 for details). Consider a 3D sample with a spatially varying RI of $n(\boldsymbol{r})$, where $\boldsymbol{r} = (x, y, z)$ represents the spatial coordinates, embedded in a uniform medium with an RI of n_m, and illuminated by a quasi-monochromatic source at the wavelength of λ. The scattering potential of the object is defined as

$$f(\boldsymbol{r}) = k_0^2\left[n(\boldsymbol{r})^2 - n_m^2\right], \tag{1}$$

where $k_0 = \frac{2\pi}{\lambda}$ is the wave vector in vacuum. Under the first Born approximation, which assumes the multiple scattering is negligible when the RI values of the sample and the medium are sufficiently close, the 3D image in Fourier space can be expressed as [16]

$$\tilde{I}(\boldsymbol{u}_\perp, u_z) \approx \tilde{I}_{DC} + \widetilde{f_{\mathrm{Re}}}(\boldsymbol{u}_\perp, u_z) H_{\mathrm{Re}}(\boldsymbol{u}_\perp, u_z) + \widetilde{f_{\mathrm{Im}}}(\boldsymbol{u}_\perp, u_z) H_{\mathrm{Im}}(\boldsymbol{u}_\perp, u_z), \tag{2}$$

where the tilde denotes quantities in the spatial frequency domain, $\boldsymbol{u}_\perp = (u_x, u_y)$ and u_z are the transverse and axial

frequencies satisfying $\sqrt{u_x^2+u_y^2+u_z^2}=\frac{1}{\lambda}$, $\tilde{I}_{DC}=\delta(\boldsymbol{u}_\perp,u_z)\int S(\boldsymbol{u}'_\perp)|P(\boldsymbol{u}'_\perp)|^2\mathrm{d}\boldsymbol{u}'^2_\perp$ is the DC term representing the background, $S(\boldsymbol{u}_\perp)$ represents the 2D source distribution, and $P(\boldsymbol{u}_\perp)$ is the pupil function of the microscope. $f_{\mathrm{Re,Im}}$ are the real and imaginary parts of the scattering potential as $f(\boldsymbol{r}_\perp,z)=f_{\mathrm{Re}}(\boldsymbol{r}_\perp,z)+jf_{\mathrm{Im}}(\boldsymbol{r}_\perp,z)$, and $H_{\mathrm{Re,Im}}$ are the non-paraxial 3D phase and absorption transfer function, respectively, given by

$$\begin{cases} H_{\mathrm{Re}}(\boldsymbol{u}_\perp,u_z)=-j\int\left[\left(\frac{S\left(\boldsymbol{u}'_\perp-\frac{1}{2}\boldsymbol{u}_\perp\right)}{4\pi u'_{z1}}+\frac{S\left(\boldsymbol{u}'_\perp+\frac{1}{2}\boldsymbol{u}_\perp\right)}{4\pi u'_{z2}}\right)\right] \\ P\left(\boldsymbol{u}'_\perp+\frac{1}{2}\boldsymbol{u}_\perp\right)P^*\left(\boldsymbol{u}'_\perp-\frac{1}{2}\boldsymbol{u}_\perp\right)\delta\left(u_z+u'_{z2}-u'_{z1}\right)\mathrm{d}\boldsymbol{u}'^2_\perp \\ H_{\mathrm{Im}}(\boldsymbol{u}_\perp,u_z)=\int\left[\left(\frac{S\left(\boldsymbol{u}'_\perp-\frac{1}{2}\boldsymbol{u}_\perp\right)}{4\pi u'_{z1}}-\frac{S\left(\boldsymbol{u}'_\perp+\frac{1}{2}\boldsymbol{u}_\perp\right)}{4\pi u'_{z2}}\right)\right] \\ P\left(\boldsymbol{u}'_\perp+\frac{1}{2}\boldsymbol{u}_\perp\right)P^*\left(\boldsymbol{u}'_\perp-\frac{1}{2}\boldsymbol{u}_\perp\right)\delta\left(u_z+u'_{z2}-u'_{z1}\right)\mathrm{d}\boldsymbol{u}'^2_\perp \end{cases}, \tag{3}$$

where $u'_{z1}=\sqrt{\frac{n_m^2}{\lambda^2}-|\boldsymbol{u}'_\perp+\frac{1}{2}\boldsymbol{u}_\perp|^2}$ and $u'_{z2}=\sqrt{\frac{n_m^2}{\lambda^2}-|\boldsymbol{u}'_\perp-\frac{1}{2}\boldsymbol{u}_\perp|^2}$. In our system, the pupil function is defined as $P(\boldsymbol{u}_\perp)=P_M(\boldsymbol{u}_\perp)e^{j\phi(\boldsymbol{u}_\perp)}$, where $P_M(\boldsymbol{u}_\perp)=circ(\frac{\lambda|\boldsymbol{u}_\perp|}{\mathrm{NA}_o})$ is a low-pass filter determined by the objective lens with numerical aperture $\mathrm{NA}_{\mathrm{det}}$, and $\phi(\boldsymbol{u}_\perp)$ is the phase profile of the DOE. Here, the DOE achieves snapshot parallel acquisition. A 3D intensity stack $I(x,y,z)$ associated with $P(\boldsymbol{u}_\perp)=P_M(\boldsymbol{u}_\perp)$ is constructed through the separation and rearrangement of spatially multiplexed images. Figure 1(d) shows the exemplary source patterns and their corresponding multifocal images of a phantom object [Fig. 1(c)].

To retrieve the volumetric RI distribution [Fig. 1(e)] from the 3D image intensity stack, the inverse problem can be solved using l_2 Tikhonov regularization:

$$\min_{\widetilde{f}_{\mathrm{Re}},\widetilde{f}_{\mathrm{Im}}}\mathcal{L}\left(\widetilde{f}_{\mathrm{Re}},\widetilde{f}_{\mathrm{Im}}\right)=\min_{\widetilde{f}_{\mathrm{Re}},\widetilde{f}_{\mathrm{Im}}}\sum_l\left\|\tilde{I}_l-\widetilde{f}_{\mathrm{Re}}H_{\mathrm{Re},l}-\widetilde{f}_{\mathrm{Im}}H_{\mathrm{Im},l}\right\|_2^2 +\alpha\left\|\widetilde{f}_{\mathrm{Re}}\right\|_2^2+\beta\left\|\widetilde{f}_{\mathrm{Im}}\right\|_2^2, \tag{4}$$

where $\mathcal{L}$ denotes the cost function, l indexes the illumination patterns corresponding to the four different polarization states, α and β are the regularization parameters. This optimization problem has a closed-form solution [Eq. (S13) in Supplement 1]. While Tikhonov regularization offers computational efficiency and robustness, it suffers from halo artifacts due to the missing cone problem [42]. These artifacts can be mitigated using stronger priors such as total variation (TV) regularization [19], which is particularly well suited for samples with piecewise-constant, yet at the cost of increased computational complexity. In our experimental results, we apply the TV regularization for beads and the Tikhonov regularization for biological samples.

3. RESULTS

A. Design, Fabrication, and Characterization of the DOE for Snapshot Multifocal Imaging

The design of the DOE phase profile comprises two main steps (see Section S3 of Supplement 1 for details). First, an iterative Fourier transform algorithm (IFTA) [43,44] is employed to compute a phase distribution that uniformly distributes energy across all diffraction orders. Second, a 2D geometric distortion is introduced to encode the required defocusing phase. The phase deviation for the (m_x,m_y)th diffraction order resulting from this distortion is given by [45,46]

$$\Phi(x,y)=2\pi\frac{m_x\Delta_x(x,y)++m_y\Delta_y(x,y)}{p_0}, \tag{5}$$

where Δ_x and Δ_y denote the displacements along the x and y axes, respectively, and p_0 is the original period of the phase profile. To generate a multifocal image comprising $N\times N$ planes with a constant axial separation of d, the lateral and horizontal displacements are

$$\begin{cases}\Delta_x(x,y)=\frac{np_0d}{\lambda}\sqrt{1-\frac{x^2+y^2}{(nf_0)^2}} \\ \Delta_y(x,y)=N\Delta_x(x,y)\end{cases}, \tag{6}$$

where f_0 is the effective focal length of the objective lens [47]. Here, we design the DOE to form a 5×6 2D grid of focal planes on the sensor, with the plane number and layout chosen to efficiently tile the available detector area while covering the desired axial range.

The DOE is fabricated on a fused silica substrate via three sequential rounds of photolithography processes (see Section S4 of Supplement 1 for details). Figure 2(a) is the photograph of a fabricated DOE. The element height $h(x,y)$ of the DOE element is related to the desired phase profile as $h(x,y)=\frac{\phi(x,y)\lambda}{2\pi(n_{fs}-1)}$, where $n_{fs}=1.4607$ is the refractive index of the fused silica at the wavelength $\lambda=532$ nm. The minimum step height between the eight quantized levels is 144 nm. The DOE is consisted of 1025×1025 pixels, each 8 μm in size. The height profile within the brown box in Fig. 2(a), covering an area of 553×391 μm^2, is measured by a 3D profilometer (Filmetrics, Profilm3D) and presented in Fig. 2(b). Figure 2(c) shows the histogram of the heights for each pixel in Fig. 2(b), clearly resolving the eight discrete thickness levels. Additional statistical data are provided in Table S1.

To validate the DOE performance, we image a 4.6 μm SiO_2 bead (Polysciences, RI = 1.43−1.46) immersed in an index-matching liquid (Cargille Refractive Index Liquid Series A, RI = 1.46) using a 40×/0.65 NA objective. The experimental setup is based on a commercial microscope (IX81, Olympus) with LED illumination (M530L4, Thorlabs) filtered by a 3 nm bandwidth laser-line bandpass filter centered at 532 nm (FL532-3, Thorlabs). A 4f system [L2 and L3 in Fig. 1(a)] composed of a 10 mm focal length lens and an aspheric condenser lens (ACL12708U-A, Thorlabs) accesses the Fourier plane of the illumination, where the QPP is inserted for SPRIT measurements. The condenser provides an effective $\mathrm{NA}_{\mathrm{illu}}=0.33$, limited by the LED source. The image is relayed through another 4f system [L4 and L5 in Fig. 1(a)]. The DOE generating the 5×6 multifocal image array with an axial step of 0.625 μm for a 40× objective is positioned at the detection-side Fourier plane. The final image is captured by a polarization CMOS camera (BFS-U3-51S5P-C, FLIR). More characterization of the DOE can be found in Section S5 of Supplement 1.

The raw image of a single SiO_2 bead is shown in Fig. 2(d). Since the object is illuminated by the unpolarized LED without QPP inserted, the camera effectively operates as a conventional unpolarized sensor. The lateral field of view (FOV) of the multifocal image is controlled by a circular iris placed at the intermediate image plane to avoid sub-image overlapping. A square aperture

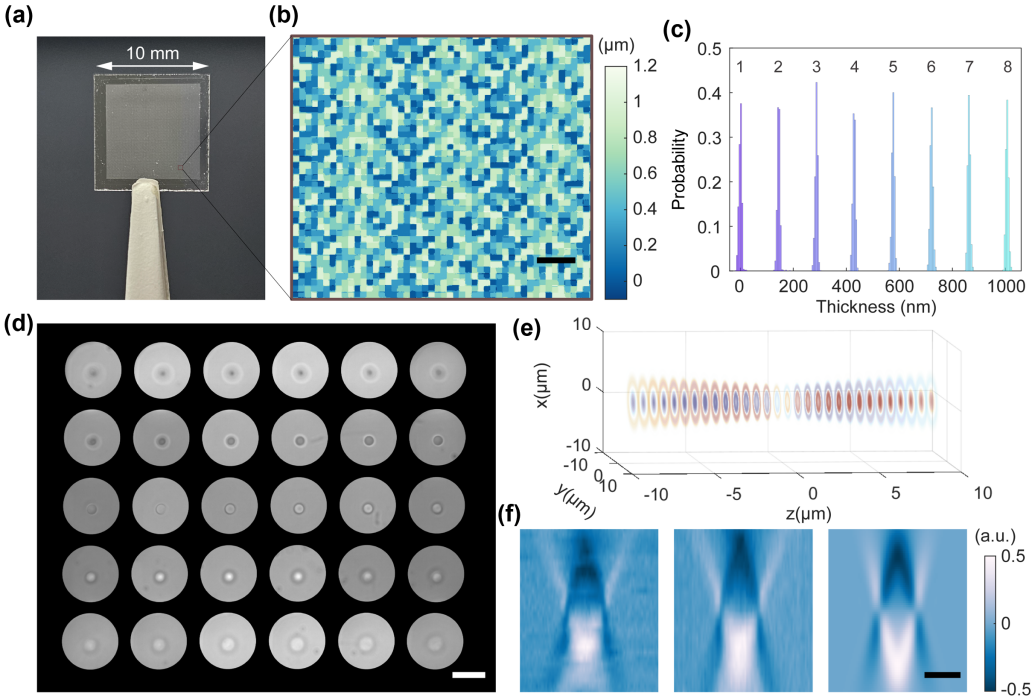

Fig. 2. Fabrication and characterization of the DOE. (a) Photograph of the 3-bit DOE fabricated by photolithography. (b) Height map of the DOE within the brown box in (a), measured by a 3D profilometer. Scale bar, 50 μm. (c) Histogram of the DOE heights, showing eight discrete thickness levels. (d) Raw image of a 4.6 μm SiO_2 bead captured by the polarization CMOS camera with the DOE positioned at the Fourier plane. Scale bar, 15 μm. (e) Thirty channels segmented from the raw image and rearranged into a 3D focal stack. (f) Comparison of x–z slices: from the rearranged snapshot measurement (left), from multiple-plane axial scanning (center), and simulation (right). Scale bar, 5 μm.

could be employed in future implementations to make full use of the detector area. The raw image is segmented into 30 sub-images, spatially aligned, and rearranged to form a 3D image stack, as illustrated in Fig. 2(e). Figure 2(f) displays the x–z cross-section of the 3D image at $y = 0$ obtained using DOE. In addition, we generate a simulated 3D stack based on the forward model in Eq. (2) and a conventional z-stack acquired via axial scanning across the same depth range for comparison. The results show strong agreement between the realigned stack from the snapshot measurement with both the simulated and conventionally acquired stacks, validating the fidelity of the DOE-enabled snapshot multifocal imaging. The weak discrete banding visible in the experimental x–z slice arises from minor misalignment of the DOE with respect to the optical axis (see Section S6 of Supplement 1 for details) and slight variation in the energy distribution across different orders.

B. Benchmarking of SPRIT with SiO_2 Beads

We demonstrate the snapshot RI tomography capability of SPRIT with the SiO_2 beads in Fig. 2(e). The QPP [Fig. 1(b)] is inserted at the Fourier plane of the illumination path to generate distinct source profiles for the four polarization channels. To assess performance across different imaging conditions, we compare results obtained using two objectives: a 20×/0.4 NA air objective and a 60×/1.2 NA water-immersion objective. The DOE generates a 5 × 6 multifocal image array with defocus steps of 1 μm and 278 nm, respectively. Representative sub-images from each polarization channel are shown in Fig. 3(a) and Fig. S4 for the low- and high-NA cases, respectively.

Figures 3(b) and 3(c) show orthogonal slices of the magnitude of phase transfer functions associated with the two objectives, averaged over the four polarization-dependent phase transfer functions. The individual phase transfer functions for each illumination pattern are shown in Fig. S5. The shape of the transfer function is determined by the ratio of the illumination and detection NA, known as the coherence parameter $\rho = \frac{\mathrm{NA_{illu}}}{\mathrm{NA_{det}}}$ [21]. The lateral frequency support of the transfer functions is extended beyond the coherent limit set by $\mathrm{NA_{det}}$, thereby improving the achievable lateral resolution. The theoretical limits of lateral and axial resolution are given by $\lambda/(\mathrm{NA_{illu}} + \mathrm{NA_{det}})$ and $\frac{2\lambda}{[(n-\sqrt{n^2-\mathrm{NA_{det}^2}})+(n-\sqrt{n^2-\mathrm{NA_{illu}^2}})]}$, respectively, where n is the RI of the immersion medium. Figures 3(d) and 3(e) illustrate the 3D RI reconstruction of SiO_2 beads with different objective lenses. The 30 multifocal planes captured by the DOE are first interpolated to 100 z-planes spanning the entire defocus range before solving the inverse problem, which improves the computation of the 3D transfer function and the numerical stability of the inverse problem. Since the sample is a pure phase object with a piecewise-constant RI distribution, TV regularization is applied. As expected, the reconstruction with a higher-NA objective yields better resolution in both lateral and axial dimensions. Both reconstructions are subject to the missing cone problem, which can lead to elongation along the z-axis and artifacts such as the halo around the sphere. This effect becomes more prominent when the coherence parameter is smaller, since reduced angular coverage enlarges the missing-cone region. Increasing the illumination NA can help mitigate this issue by expanding frequency coverage [48]. In addition, incorporating stronger priors such as non-negativity of the RI contrast can further suppress missing-cone artifacts [42]. Deep learning-based reconstruction methods have also been explored to address this limitation [49,50].

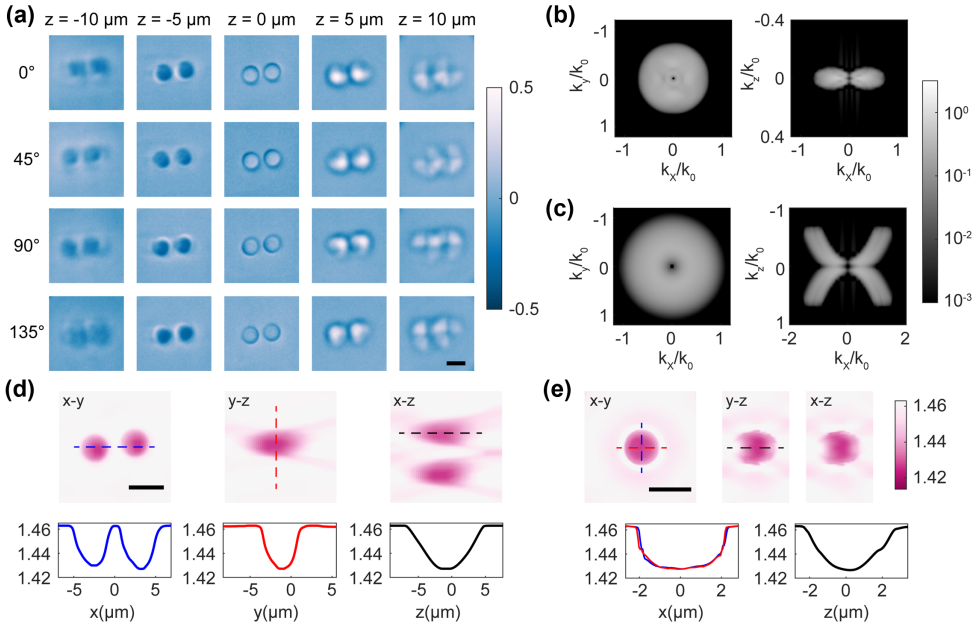

Fig. 3. Benchmarking of SPRIT with SiO_2 beads. (a) Segmented SPRIT measurements of 4.6 μm SiO_2 beads suspended in index-matching oil (RI = 1.46) by a 20 × 0.4 NA air objective. Sub-images of the four polarization channels, focused on five different axial planes, are shown. Scale bar: 5 μm. (b, c) Orthogonal slices of the magnitude of the phase transfer function, averaged over the four polarization-dependent phase transfer functions of the SPRIT system with (b) a 20 × 0.4 NA air objective and (c) a 60 × 1.2 NA water-immersion objective, respectively. (d, e) Reconstructed refractive index maps and cross-sectional slices corresponding to (b) and (c), respectively. Scale bar: 5 μm.

C. 3D RI Imaging of Spirogyra

We demonstrate the effectiveness of SPRIT on a *Spirogyra* sample (Carolina Biological Supply), embedded in fresh water (RI = 1.33). *Spirogyra* is a filamentous unicellular algae composed of a chain of cylindrical cells connected end-to-end, each containing a centrally located nucleus and helically arranged chloroplasts oriented in 3D space.

To capture the full extent of a single cell, we stitch 16 raw measurements, which are acquired using a 20 × /0.4 NA objective lens while laterally scanning along the cell. RI reconstruction is performed using Tikhonov regularization. The final volumetric reconstruction comprises 300 × 1711 × 100 voxels, corresponding to a physical volume of 52 × 295 × 71 μm^3. A 3D rendering of the reconstructed RI distribution is shown in Fig. 4(a). Representative x–y slices at depths of $z = 16, 36, 49$ μm are presented in Fig. 4(b), revealing details of the upper and lower chloroplast layers within a single cell, as well as the intersection with an adjacent filament. Figure 4(c) presents x–z slices at x = 14 and 34 μm, clearly depicting the characteristic spiral arrangement of the chloroplasts. A magnified view of the boxed region in Fig. 4(b), highlighting the cell nucleus, is shown in Fig. 4(d). Line profiles along the red and black dashed lines in Fig. 4(b), corresponding to the top and bottom layers of chloroplasts at the same y position, are plotted in Fig. 4(e). The RI profile extracted along the orange dashed line in Fig. 4(d) is shown in Fig. 4(f).

D. Dynamic 3D RI Imaging of Live Cells

We further showcase the snapshot, label-free 3D imaging capability of SPRIT on dynamic biological samples. Figure 5 and Visualization 1 show the time-resolved RI distribution of a live *Chilomonas* cell (Carolina Biological Supply), suspended in spring water (RI = 1.33). We captured its flagellar motion, observing rapid oscillations followed by reorientation, during which one flagellum remained anchored to the coverslip while the other actively drove the motion. SPRIT provides a powerful platform for investigating the 3D swimming behavior and flagellar beating patterns of diverse protist species. Imaging is performed using a 40 × /0.65 NA objective at 50 Hz over a duration of 1.1 s.

Figure 5(a) presents 3D renderings of the RI distribution at selected time points, highlighting key cellular postures throughout the rotation process. The reconstruction comprises 300 × 300 × 100 voxels, corresponding to a physical volume of 26 × 26 × 19 μm^3. The volumes in Fig. 5(a) and Visualization 1 are rendered by ClearVolume [51]. Representative x–y slices at three distinct axial planes are shown in Fig. 5(b), demonstrating good optical-sectioning capability. The boundary visible near the periphery of the slices originates from the iris used to control the FOV. The white and orange arrows in the last row indicate the anchored and moving flagella, respectively.

We further examine the flagellum in the green box in Fig. 5(a). Figure 5(c) shows a zoomed 3D rendering with display contrast adjusted for visualization. The reported diameter of *Chilomonas* flagella is approximately 150 nm [52], which is below the resolution limit of our system. Consequently, the reconstructed flagellar cross-section primarily reflects system broadening rather than the true physical diameter. The s–z slice extracted along the white line in Fig. 5(c) is shown in Fig. 5(d), where s denotes the direction perpendicular to the flagellar axis. Line profiles across the flagellum [Fig. 5(e)] yield full widths at half maximum (FWHM) of 0.64 μm laterally and 3.36 μm axially. We note that the recovered RI value of the flagellum is lower than its true value, as spatial blurring reduces the apparent RI contrast of sub-resolution features.

Figure 5(f) displays the orthogonal views (x–y, x–z, and y–z) of the reconstructed 3D volume at $t = 0.02$ s. The y–z slice reveals a tilted cell body relative to the x–y plane. Line profiles along the red

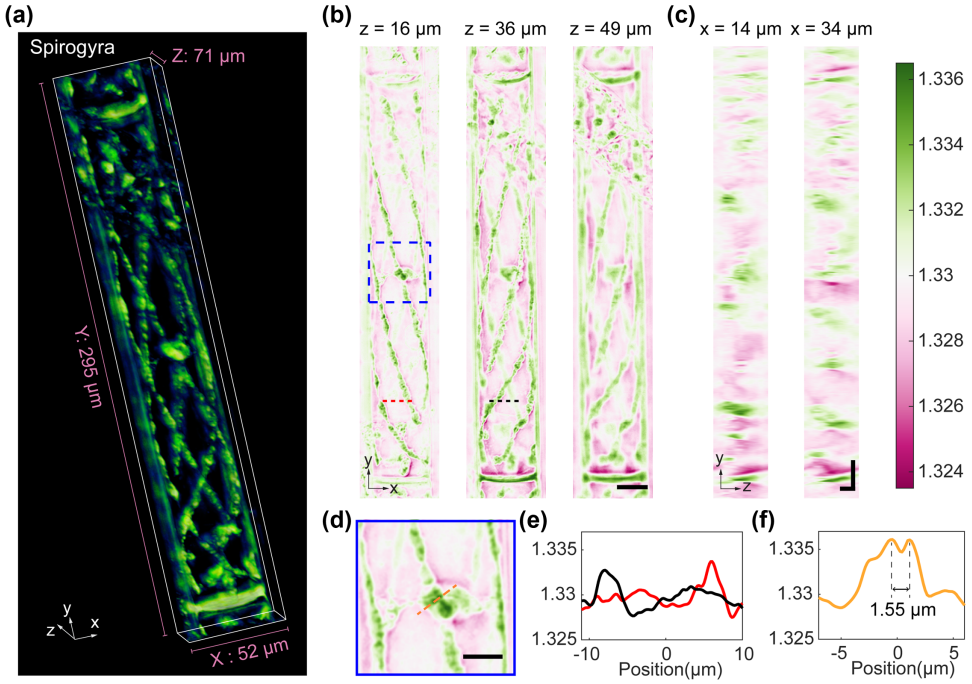

Fig. 4. Tomographic imaging of *Spirogyra*. (a) 3D rendering of the RI distribution of *Spirogyra*. (b) x–y plane slices at $z = 16$, 36, and 49 μm. Scale bar, 20 μm. (c) y–z plane slices at $x = 14$ and 34 μm. Scale bar, 20 μm. Note that the lateral and axial scale bars are different. (d) Zoomed-in image of the nucleus in the blue dashed box in (a). Scale bar, 10 μm. (e) Line profiles extracted along the red and black dashed lines in (b). (f) Line profiles extracted along the orange dashed lines in (d), demonstrating the ability of SPRIT to resolve subcellular structures.

dashed lines in Figs. 5(b) and 5(f) are plotted in Fig. 5(g). These profiles indicate a lateral feature of 0.59 μm and an axial feature of 3.44 μm. Both single-feature and two-feature characterizations are consistent with the theoretical lateral and axial resolution limits derived in Section 3.B. Figure 5(h) shows the orthogonal slices of the 3D Fourier spectrum of the reconstructed RI volume, which exhibits cutoff frequencies consistent with these resolution limits. The high spatial and temporal resolution achieved by SPRIT enables detailed observation of rapid morphological changes in live, label-free cells, making it well suited for applications in cellular dynamics and microbial motility studies.

4. DISCUSSION AND CONCLUSION

In our demonstration of SPRIT, all the multifocal images are distributed across the entire FOV without any overlap on a single polarization camera. The total number of resolvable voxels is therefore limited by the size of the camera sensor. The selection of the number of axial planes depends on the depth of field (DOF) of the imaging system and the axial range of the object of interest. Since we employed a 3D forward model, to avoid aliasing in the axial direction, the defocus step d should be smaller than approximately half of the system DOF, while the product of the total number of sub-images and d should exceed the axial extent of the object. While SPRIT enables high spatial resolution, a small sensor inherently limits the observable volume. To overcome this, multiple cameras, each configured to capture multifocal images centered at different axial depths, can be employed in parallel to expand the total detection volume without sacrificing the single-shot capability. Additionally, compressed sensing–based reconstruction [53] could be employed to recover 3D volumes from partially overlapping sub-images [54], further increasing spatial throughput. It is worth noting that increasing spatial overlap leads to reduced measurement contrast and a lower signal-to-noise ratio. Therefore, a trade-off between enhancing the system throughput and preserving adequate contrast is necessary to ensure high-fidelity reconstruction.

Other than the sensor area and overlap, the 3D transfer functions govern both the information throughput and the contrast of the captured images. Optimizing the source illumination patterns using techniques such as simulated annealing [55] or physics-informed learning frameworks [56] can improve spatial frequency coverage and minimize reconstruction artifacts. On the detection side, improvements in the DOE design may involve encoding more complex and distinguishable phase profiles beyond simple defocus, allowing for more efficient sampling of the 3D volume. Alternatively, the DOE can be replaced by metasurfaces, which offer more design degree of freedom and can be tailored for polarization-dependent pupil functions [57]. Further improvements could be achieved through end-to-end optimization strategies [58,59], where the transfer function and reconstruction algorithm are jointly designed to maximize information encoding and recovery efficiency. It should be noted that the current reconstruction model assumes a polarization-insensitive sample, which is valid for common biological specimens. SPRIT may be extended to polarization-sensitive tomography for anisotropic samples by incorporating the RI tensor of the sample into the forward model [60,61].

In conclusion, we propose SPRIT, a single-shot 3D RI imaging technique based on a DOE which generates multifocal intensity images. SPRIT incorporates polarization-multiplexed partially coherent illumination and reconstructs 3D RI distributions using a regularized 3D deconvolution algorithm. The DOE is alignment-insensitive and compatible with various microscope

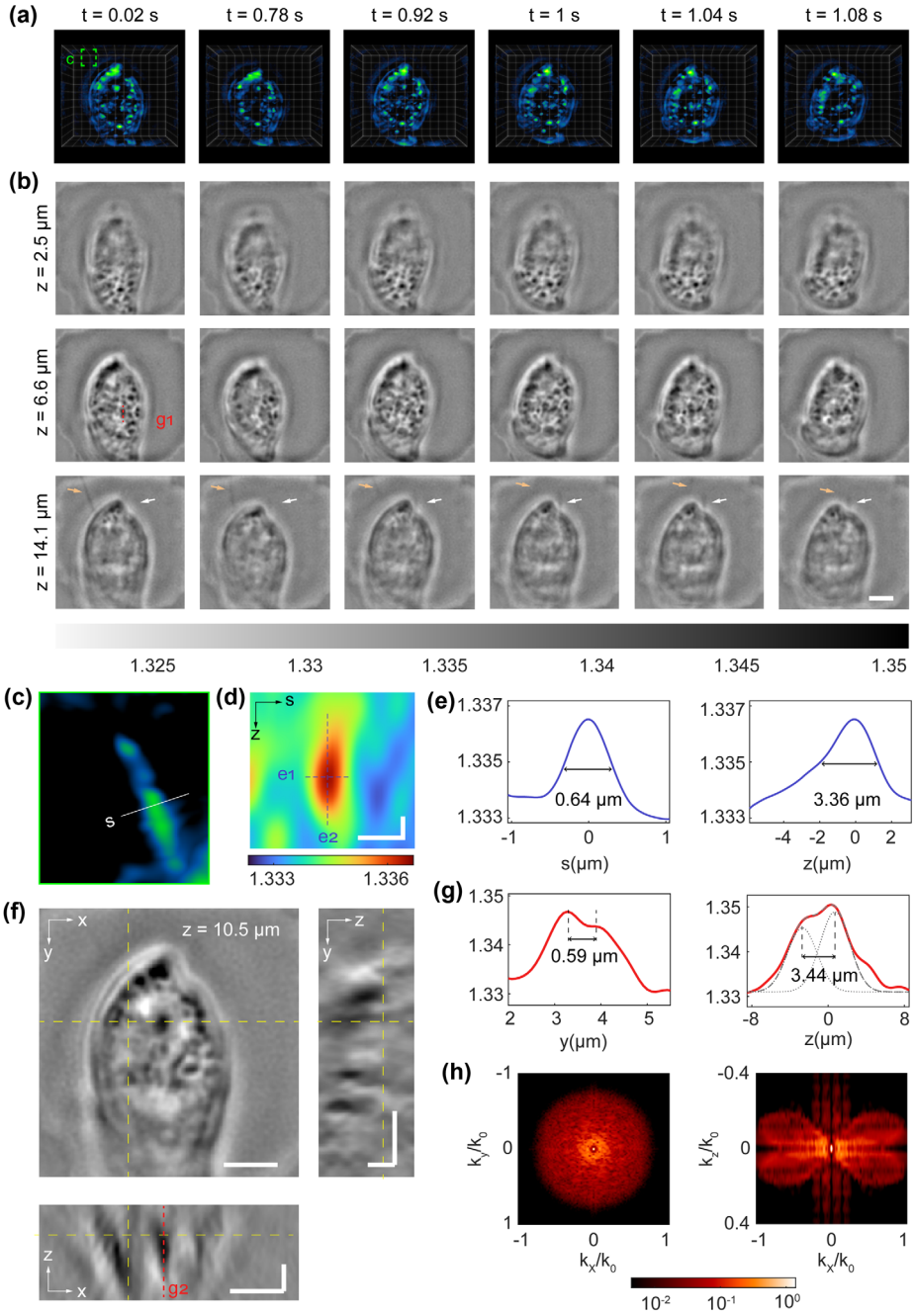

Fig. 5. Dynamic 3D refractive index imaging of a live *Chilomonas*. (a) 3D RI distributions of a live *Chilomonas* at selected time points, as indicated at the top. See Visualization 1 for the corresponding 3D dynamics video. The video was recorded at 50 Hz. (b) Representative x–y plane slices at multiple axial positions. Scale bar: 5 μm. The white and orange arrows in the last row indicate the anchored and moving flagella, respectively. (c) Zoomed 3D rendering of the flagellum within the green box in (a). Display contrast is adjusted for visualization. (d) s–z slice through the flagellum extracted along the white line in (c), where s denotes the direction perpendicular to the flagellum axis. Scale bar: 2 μm. Note that the lateral and axial scale bars are different. (e) RI profiles across the flagellum along the blue dashed lines in (d). (f) Orthogonal views of the reconstructed 3D volume (x–y, x–z, and y–z planes) at $t = 0.02$ s. Scale bar: 5 μm. (g) Line profiles extracted along the red dashed lines in (b) and (f). The axial profile (right) is fitted with a sum of two Gaussian functions (individual components shown as dotted lines; sum shown as dashed line) to estimate the feature size along z direction. (h) Orthogonal slices of the 3D Fourier spectrum of the reconstructed RI volume.

objectives, enabling seamless integration into commercial imaging platforms. Compared with conventional or other snapshot RI tomography techniques, SPRIT achieves both high spatial and temporal resolution. Beyond live cell imaging, SPRIT also holds promise for optical data storage [62], where high-speed, precise volumetric readout is essential. Moreover, the optical system can be further engineered to encode additional information of light, such as spectrum [63] and polarization [64]. With its scalability, robustness, and ease of integration, SPRIT is well positioned for widespread adoption across biological, biomedical, and photonics research.

Funding. National Science Foundation (ECCS-2320437, 2348536).

Acknowledgment. The author would like to thank Ruixuan Zhao and Xiang Dai for their discussion on this work.

Disclosures. The authors declare no conflicts of interest.

Data availability. Data underlying the results presented in this paper are not publicly available at this time but may be obtained from the authors upon reasonable request.

Supplemental document. See Supplement 1 for supporting content.

REFERENCES

1. "Milestones in light microscopy," Nat. Cell Biol. **11**, 1165 (2009).
2. I. A. Hatton, E. D. Galbraith, N. S. C. Merleau, *et al.*, "The human cell count and size distribution," Proc. Natl. Acad. Sci. USA **120**, e2303077120 (2023).
3. T. A. Zangle and M. A. Teitell, "Live-cell mass profiling: an emerging approach in quantitative biophysics," Nat. Methods **11**, 1221–1228 (2014).
4. F. Zernike, "How I discovered phase contrast," Science **121**, 345–349 (1955).
5. W. Lang, *Nomarski Differential Interference-Contrast Microscopy* (Carl Zeiss Oberkochen, 1982).
6. G. Popescu, *Quantitative Phase Imaging of Cells and Tissues* (McGraw-Hill Education, 2011).
7. Y. Park, C. Depeursinge, and G. Popescu, "Quantitative phase imaging in biomedicine," Nat. Photonics **12**, 578–589 (2018).
8. T. L. Nguyen, S. Pradeep, R. L. Judson-Torres, *et al.*, "Quantitative phase imaging: recent advances and expanding potential in biomedicine," ACS Nano **16**, 11516–11544 (2022).
9. G. A. Dunn and D. Zicha, "Phase-shifting interference microscopy applied to the analysis of cell behaviour," Symp. Soc. Exp. Biol. **47**, 91–106 (1993).
10. P. Marquet, B. Rappaz, P. J. Magistretti, *et al.*, "Digital holographic microscopy: a noninvasive contrast imaging technique allowing quantitative visualization of living cells with subwavelength axial accuracy," Opt. Lett. **30**, 468–470 (2005).
11. B. Bhaduri, C. Edwards, H. Pham, *et al.*, "Diffraction phase microscopy: principles and applications in materials and life sciences," Adv. Opt. Photonics **6**, 57–119 (2014).
12. G. Zheng, R. Horstmeyer, and C. Yang, "Wide-field, high-resolution Fourier ptychographic microscopy," Nat. Photonics **7**, 739–745 (2013).
13. M. R. Teague, "Deterministic phase retrieval: a Green's function solution," J. Opt. Soc. Am. **73**, 1434–1441 (1983).
14. D. Paganin and K. A. Nugent, "Noninterferometric phase imaging with partially coherent light," Phys. Rev. Lett. **80**, 2586–2589 (1998).
15. L. Tian and L. Waller, "Quantitative differential phase contrast imaging in an LED array microscope," Opt. Express **23**, 11394–11403 (2015).
16. N. Streibl, "Three-dimensional imaging by a microscope," J. Opt. Soc. Am. A **2**, 121–127 (1985).
17. M. H. Jenkins and T. K. Gaylord, "Three-dimensional quantitative phase imaging via tomographic deconvolution phase microscopy," Appl. Opt. **54**, 9213–9227 (2015).
18. J. M. Soto, J. A. Rodrigo, and T. Alieva, "Label-free quantitative 3D tomographic imaging for partially coherent light microscopy," Opt. Express **25**, 15699–15712 (2017).
19. M. Chen, L. Tian, and L. Waller, "3D differential phase contrast microscopy," Biomed. Opt. Express **7**, 3940–3950 (2016).
20. J. M. Soto, J. A. Rodrigo, and T. Alieva, "Optical diffraction tomography with fully and partially coherent illumination in high numerical aperture label-free microscopy [Invited]," Appl. Opt. **57**, A205–A214 (2018).
21. J. Li, Q. Chen, J. Sun, *et al.*, "Three-dimensional tomographic microscopy technique with multi-frequency combination with partially coherent illuminations," Biomed. Opt. Express **9**, 2526–2542 (2018).
22. E. Wolf, "Three-dimensional structure determination of semi-transparent objects from holographic data," Opt. Commun. **1**, 153–156 (1969).
23. V. Lauer, "New approach to optical diffraction tomography yielding a vector equation of diffraction tomography and a novel tomographic microscope," J. Microsc. **205**, 165–176 (2002).
24. W. Choi, C. Fang-Yen, K. Badizadegan, *et al.*, "Tomographic phase microscopy," Nat. Methods **4**, 717–719 (2007).
25. P. Bon, G. Maucort, B. Wattellier, *et al.*, "Quadriwave lateral shearing interferometry for quantitative phase microscopy of living cells," Opt. Express **17**, 13080–13094 (2009).
26. H. Kwon, E. Arbabi, S. M. Kamali, *et al.*, "Single-shot quantitative phase gradient microscopy using a system of multifunctional metasurfaces," Nat. Photonics **14**, 109–114 (2019).
27. J. Zhou, Q. Wu, J. Zhao, *et al.*, "Fourier optical spin splitting microscopy," Phys. Rev. Lett. **129**, 020801 (2022).
28. Q. Wu, J. Zhou, X. Chen, *et al.*, "Single-shot quantitative amplitude and phase imaging based on a pair of all-dielectric metasurfaces," Optica **10**, 619–625 (2023).
29. L. Li, S. Wang, F. Zhao, *et al.*, "Single-shot deterministic complex amplitude imaging with a single-layer metalens," Sci. Adv. **10**, eadl0501 (2024).
30. L. Li, W. Jia, C. Jin, *et al.*, "Single-shot wavefront sensing with nonlocal thin film optical filters," Laser Photonics Rev. **17**, 2300426 (2023).
31. J. Li, Y. Li, T. Gan, *et al.*, "All-optical complex field imaging using diffractive processors," Light Sci. Appl. **13**, 120 (2024).
32. A. Kuś, "Real-time, multiplexed holographic tomography," Opt. Lasers Eng. **149**, 106783 (2022).
33. S. K. Mirsky, I. Barnea, and N. T. Shaked, "Dynamic tomographic phase microscopy by double six-pack holography," ACS Photonics **9**, 1295–1303 (2022).
34. Y. Sung, "Snapshot holographic optical tomography," Phys. Rev. Appl. **11**, 014039 (2019).
35. B. Xiong, X. Li, Y. Zhou, *et al.*, "Snapshot partially coherent diffraction tomography," Phys. Rev. Appl. **15**, 044048 (2021).
36. J. Wang, X. Zhao, Y. Wang, *et al.*, "Quantitative real-time phase microscopy for extended depth-of-field imaging based on the 3D single-shot differential phase contrast (ssDPC) imaging method," Opt. Express **32**, 2081–2096 (2024).
37. A. Descloux, K. S. Grußmayer, E. Bostan, *et al.*, "Combined multi-plane phase retrieval and super-resolution optical fluctuation imaging for 4D cell microscopy," Nat. Photonics **12**, 165–172 (2018).
38. Z. F. Phillips, M. Chen, and L. Waller, "Single-shot quantitative phase microscopy with color-multiplexed differential phase contrast (cDPC)," PLOS ONE **12**, e0171228 (2017).
39. C. Lee, H. Hugonnet, J. Park, *et al.*, "Single-shot refractive index slice imaging using spectrally multiplexed optical transfer function reshaping," Opt. Express **31**, 13806–13816 (2023).
40. H. Yoon, H. Chae, K. C. Lee, *et al.*, "Single-shot Fourier ptychography using polarization-encoded illumination," Appl. Phys. Lett. **126**, 123702 (2025).
41. M. Born and E. Wolf, *Principles of Optics: Electromagnetic Theory of Propagation, Interference and Diffraction of Light* (Elsevier, 2013).
42. J. Lim, K. Lee, K. H. Jin, *et al.*, "Comparative study of iterative reconstruction algorithms for missing cone problems in optical diffraction tomography," Opt. Express **23**, 16933–16948 (2015).
43. O. Ripoll, V. Kettunen, and H. P. Herzig, "Review of iterative Fourier-transform algorithms for beam shaping applications," Opt. Eng. **43**, 2549–2556 (2004).
44. F. Wyrowski, "Iterative quantization of digital amplitude holograms," Appl. Opt. **28**, 3864–3870 (1989).
45. P. M. Blanchard and A. H. Greenaway, "Simultaneous multiplane imaging with a distorted diffraction grating," Appl. Opt. **38**, 6692–6699 (1999).
46. S. Abrahamsson, J. Chen, B. Hajj, *et al.*, "Fast multicolor 3D imaging using aberration-corrected multifocus microscopy," Nat. Methods **10**, 60–63 (2013).
47. E. J. Botcherby, R. Juskaitis, M. J. Booth, *et al.*, "Aberration-free optical refocusing in high numerical aperture microscopy," Opt. Lett. **32**, 2007–2009 (2007).
48. C. Zuo, J. Li, J. Sun, *et al.*, "Transport of intensity equation: a tutorial," Opt. Lasers Eng. **135**, 106187 (2020).
49. K. C. Zhou and R. Horstmeyer, "Diffraction tomography with a deep image prior," Opt. Express **28**, 12872–12896 (2020).
50. H. Chung, J. Huh, G. Kim, *et al.*, "Missing cone artifact removal in ODT using unsupervised deep learning in the projection domain," IEEE Trans. Comput. Imaging **7**, 747–758 (2021).
51. L. A. Royer, M. Weigert, U. Günther, *et al.*, "ClearVolume: open-source live 3D visualization for light-sheet microscopy," Nat. Methods **12**, 480–481 (2015).
52. H. P. Brown and A. Cox, "An electron microscope study of protozoan flagella," Am. Midl. Nat. **52**, 106–117 (1954).

53. D. L. Donoho, "Compressed sensing," IEEE Trans. Inf. Theory **52**, 1289–1306 (2006).
54. R. Malik and K. Khare, "Single-shot extended field of view imaging using point spread function engineering," J. Opt. Soc. Am. A **40**, 1066–1075 (2023).
55. H. Hugonnet, M. Lee, and Y. Park, "Optimizing illumination in three-dimensional deconvolution microscopy for accurate refractive index tomography," Opt. Express **29**, 6293–6301 (2021).
56. R. Cao, M. Kellman, D. Ren, *et al.*, "Self-calibrated 3D differential phase contrast microscopy with optimized illumination," Biomed. Opt. Express **13**, 1671–1684 (2022).
57. B. Xiong, Y. Liu, Y. Xu, *et al.*, "Breaking the limitation of polarization multiplexing in optical metasurfaces with engineered noise," Science **379**, 294–299 (2023).
58. Z. Lin, C. Roques-Carmes, R. Pestourie, *et al.*, "End-to-end nanophotonic inverse design for imaging and polarimetry," Nanophotonics **10**, 1177–1187 (2021).
59. E. Tseng, S. Colburn, J. Whitehead, *et al.*, "Neural nano-optics for high-quality thin lens imaging," Nat. Commun. **12**, 6493 (2021).
60. A. Saba, J. Lim, A. B. Ayoub, *et al.*, "Polarization-sensitive optical diffraction tomography," Optica **8**, 402–408 (2021).
61. S. Song, J. Kim, T. Moon, *et al.*, "Polarization-sensitive intensity diffraction tomography," Light Sci. Appl. **12**, 124 (2023).
62. H. Wang, Y. Lei, L. Wang, *et al.*, "100-layer error-free 5D optical data storage by ultrafast laser nanostructuring in glass," Laser Photonics Rev. **16**, 2100563 (2022).
63. Q. Cui, J. Park, Y. Ma, *et al.*, "Snapshot hyperspectral light field tomography," Optica **8**, 1552–1558 (2021).
64. Z. Shen, F. Zhao, C. Jin, *et al.*, "Monocular metasurface camera for passive single-shot 4D imaging," Nat. Commun. **14**, 1035 (2023).